AN INVERSE DESIGN METHOD FOR AIRCRAFT ENGINE SAND SEPARATOR SYSTEM

Farooq Saeed and Ahmed Z. Al-Garni

Aerospace Engineering Department, King Fahd University of Petroleum & Minerals, Dhahran 31261, Saudi Arabia

An Extended Abstract

An Abstract for presentation at the

28th European Rotorcraft Forum

Amsterdam, the Netherlands, 4-7 September 2012

Summary

This paper presents the details of development of an efficient design method for aircraft engine sand separator systems. The development of such a method was felt necessary to address the problem of sand ingestion since it is a vital concern for the regional aviation community because of the desert environment as it can seriously affect the operation, performance and life cycle of a turbine engine employed for aviation or industrial applications. The design method makes use of state-of-the-art and practical design and analysis techniques, such as the inverse aerodynamic design methodology that also takes into account viscous effects to aid in the design of specific profile shapes for engine air intakes. The sand separator design is achieved by giving a specific contour to the intake profile (such as a highly curved bend in the duct) that the contaminants because of their inertial momentum are forced away from the central flow. Since the sand particles can rebound of the air intake walls and enter the engine, the method takes into account sand particle rebound or restitution characteristics in the design. The design is accomplished with the aid of optimization techniques in both the inverse aerodynamic design as well as in the sand separator system design. In addition, to facilitate the design, several numerical programs and graphical user interface have been developed to aid in the design and analysis of aircraft engine sand separator systems in an interactive manner. Several design examples are presented to demonstrate the usefulness and utility of the method

1. Introduction

Saudi Arabia is known to have a harsh desert-like environment in most of its regions. The air in these environments is usually laden with sand and dust particles. Aircrafts operating under such conditions for long periods are vulnerable to internal engine damage. Saudi Arabia also generates its electricity

entirely from one of the largest fleet of gas turbine engines. Sand ingestion is, therefore, a vital concern for the regional aviation (Saudi Arabian Airlines, NAS Air, Saudi Aramco Aviation and private aviation companies) and power generation authorities (Saudi Electricity Company) since sand can seriously affect the operation and performance of a turbine engine that is being used either for aviation or for industrial applications such as power generation. The operational life of a turbine engine operating in sandy environments can be as short as 50 hours [1, 2]. Engine damage ranges from simple erosion in the engine blades, to a completely inoperative engine with as little as half a pound of sand [3]. In addition, the degradation in performance and efficiency of the turbine engine leads to increases in fuel consumption and operational cost [1].

Aramco Aviation, which provides major aerial transportation support services to Saudi Aramco, the biggest oil company in the world, operates both fixed and rotary-wing aircraft out of sand/desert strips in remote oil and gas fields spread all over the region. Aramco Aviation experience in operating from these remote areas has evidenced significant performance degradation and lifetime reduction of its aircraft turbine engines primarily due to sand erosion. Figures 1(a) and (b) provided by Aramco Aviation [4] reveal the harmful effects of sand erosion on turbine vanes and blades, respectively. They attribute this damage to the presence of fine dust and sand together with high moisture content in the region. Aramco Aviation also had to prematurely remove all of the engines from its fleet of Dash-8 aircraft within the first year of its service (about 1,000 hours) due to damage caused by sand ingestion. In addition, aircraft air conditioning and filtration systems were also amongst the major areas affected by the sand particles which without adequate maintenance specific to the regional environment were found to survive only one-fifth of their expected life.

As evident from Fig. 1, physical examination of the effects of sand erosion reveals blunted leading edges, sharpened trailing edges, reduced blade chords, and increased pressure surface roughness, to name a few. It, therefore, becomes imperative that some form of protective device, such as an Inertial Particle Separator (IPS) system, must be employed in the air intake of turbine engines operating in desert environment to prolong their operational life and to provide sustained performance. Thus, the use of an IPS system is a recommended practice in desert-like environments. Studies [5, 6] have found erosion in turbo-machinery to be principally related to the **gas flow path** and **sand particle size**, and to a lesser degree to other factors such as the ingested sand particle characteristics, blade geometry, internal engine passages, environmental and operating conditions, and blade material.

(a) High pressure turbine vanes

(b) High pressure turbine blades

Figure 1: Effects of sand erosion on high pressure turbine (a) vanes and (b) blades of aircraft engines operating in the Saudi Arabian desert environment. (Courtesy: Tariq Jabr, Saudi Aramco Aviation)

Currently there are two types of IPS systems in use: the swirl and the vaneless type. In the swirl type, vanes introduce a swirl to the contaminated inlet flow. The resulting centrifugal force causes the heavier sand particles to move over to the outer periphery and into a scavenge duct. The vaneless type

relies on the specific contour of the inner walls of the inlet and the diffuser that direct the contaminants to the scavenge duct.

Figure 2: Boeing CH-47D helicopter with an IPS system installed [3].

Figure 2 [3] shows a Boeing CH-47D helicopter with the IPS system installed (shown inside the circle) on the engine inlets. The engine-mounted particle separator is an axisymmetric, bifurcated duct of the form shown in Fig. 3 (adapted from Ref. [3]). The different IPS systems available today are very similar in design. Contaminated air enters the device through the inlet annulus on the left, and around a sharp bend, B. The bend is designed in such a manner that the inertia of the contaminants is sufficient to prevent them from following the air around the bend. Thus contaminants, such as sand, dust, etc., pass into a scavenge passage, A, and the contaminant-free clean air passes into the engine along the inner annulus.

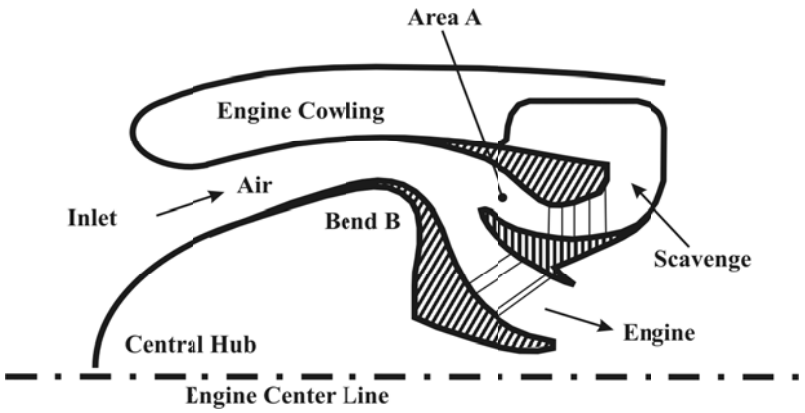

Figure 3: Typical axisymmetric helicopter engine particle separator (Adapted from Ref. [3]).

The IPS system does a phenomenal job of keeping the engines clean and free from damage due to sand particles and other foreign object ingestion. Inertial particle separator systems (such as that shown in

Fig. 3) are capable of moving large particles leaving the smaller ones to be trapped by the filters which greatly enhanced the life of the filter and offers maximum engine protection [3]. The main advantage is the large installed area required for such a system thus increasing the overall intake area. However, engines having IPS installed prevents the crew from conducting a thorough pre-flight of the engine inlet area.

However, recent military operations in the Middle East have raised the problem of inefficiency of existing IPS system designs [7] and suggest that the IPS system designs were not specifically tailored to the local or regional environmental conditions. A survey of existing design techniques for IPS system reveals that these design techniques are very costly since they make use of extensive direct analysis techniques along with experimental validation [8–10] whereby the IPS system geometry is continuously improved via numerous iterations, i.e., through hit-and-trial. In addition, the designs were not specifically tailored to the Middle Eastern or Gulf environment.

Owing to the shortcomings of the current design techniques, the current study presents a **novel and more efficient design method** for the design of an IPS system in that the design is accomplished in a single step not via direct geometry specification but through specification of the design requirements (engine mass flow rate, flight conditions, etc.) and constraints on the geometry (**gas flow path**, **sand particle size**, nacelle size, etc.) in an **inverse** fashion as opposed to the direct hit-and-trial technique. A recent study [11] has shown that solid particle erosion in turbines can be reduced by using suitable nozzle passage design to control the particle impacting velocity and impacting angle. In an inverse design, particle impact characteristics can be used as a constraint on the design resulting in a geometry that is safe from erosion. Another important and unique advantage and strength of the inverse design technique is in its **multi-point design capability** [12–15] in which multiple design requirements can be met simultaneously and, hence, the designed geometry performs equally well under "on- or off-design" conditions. Furthermore, the design method fully incorporates sand **particle rebound characteristics** as well as **viscous effects** in the design making it a very reliable tool for trade-off and practical design studies.

In the sections that follow, a brief review of literature is presented followed by details of the design methodology and its implementation. Next, parametric studies highlight some of strengths of the method followed by a few design examples. Finally, the paper ends with main conclusions of the study and its future direction.

2. Literature Review

In literature, numerous methods for the analysis and design of a sand particle system have been used [8–11] to improve the collection or scavenge efficiency of such systems and achieve high levels of reliability and durability. The methods take advantage of advanced analytical and computational (CFD)

techniques for through-flow and particle trajectory analysis. Improvements in existing design are achieved through extensive analysis and experimental validation as in the case of Ref. [8] whereby the IPS system geometry is continuously improved via numerous iterations. Thus, the design is accomplished in a direct or hit-and-trial fashion and suggests that significant amount of resources are required to accomplish the task. To overcome the limitations of the existing IPS system design methods, the on-going research effort [16, 17] aims at developing an inverse design methodology based on a new multipoint inverse design approach [12–15] for the IPS systems as opposed to the existing hit-and-trial direct design approaches.

In an inverse design method, the design is accomplished in a single step not via direct geometry specification but through specification of the design requirements which in the case of an IPS system could be the engine mass flow rate and flight conditions, and geometrical constraints on the geometry such as the gas flow path, or sand particle size, nacelle size for reduced drag. A recent study [11] has shown that solid particle erosion in turbines can be reduced by using suitable nozzle passage design to control the particle impacting velocity and impacting angle. In an inverse design, particle impact characteristics can be used as a constraint on the design resulting in a geometry that is safe from erosion. Another important and unique advantage and strength of the inverse design technique is in its multi-point design capability [12–15] in which multiple design requirements can be met simultaneously and, hence, the designed geometry performs equally well under "on- or off-design" conditions. Furthermore, the design method fully incorporates sand particle rebound characteristics as well as viscous effects in the design, making it a fast and reliable tool for trade-off and practical design studies.

A key requirement for an efficient design of an IPS system is the knowledge of sand particle characteristics which may be specific to the region. Sand in nature is composed of fine rock and mineral particles that have been altered by chemical and environmental conditions, and affected by processes such as weathering or erosion. With all the diversity in soil, sand grains are typically made up of silica or its polymorphs such as quartz. In geology, sand is categorized as a soil grain with a predefined particle size and range without consideration of the type of grain material. Many soil grain size distribution standards exist in geology and engineering where sand grain is classified in the range from 0.06 mm to 4.75 mm (60 – 4750 μm or microns). A further sub-classification defines fine sand of size 0.06 – 0.425 mm, medium between 0.425 – 2.0 mm and coarse between 2.0 – 4.75 mm. The military standard MIL E-5007C (C Spec.) classifies sand particle size between 40 μm (fine) and 800 μm (coarse). Figure 4 demonstrates a map of soil grain sizes in the Middle East [7]. A number of studies have been performed to present the particle size spectra in different areas of the Middle East. Abolkhair [18] reported the fine sand grains (0.20-0.3 mm diameter) in the Oasis of Al-Hasa, Eastern Province of Saudi Arabia. In another study, Eases [19] reported fine and medium sand (0.075-0.25 μm diameter) in their samplings in Saudi Arabia.

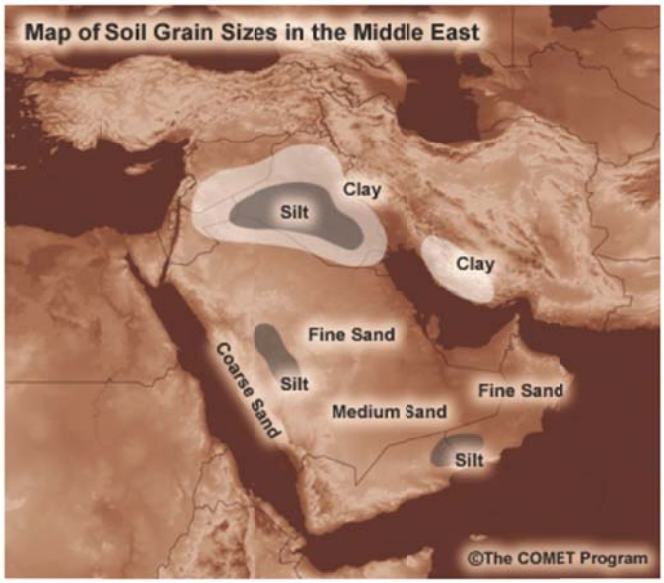

Figure 4: Map of soil grain sizes in the Middle East. Courtesy of National Center for Atmospheric Research (NCAR). Adapted from Ref. [7]

Another important consideration in the design of an IPS system is the drag of the sand particles. In studies related to sand particles, a common practice is to use some form of empirical correlation for the drag coefficient of particle. Figure 5 shows a comparison of sphere drag coefficient empirical correlations proposed by various authors [20–28]. As evident from the figure, all of the correlations agree upto a Re = 1000. In the sphere drag measurement experiments, the terminal velocity of falling spheres in stagnant medium (air or fluid) was measured. For this terminal velocity, the drag force is equal to the weight force less the buoyancy force. With this data, it is easy to determine the drag coefficient C_d for various Reynolds numbers.

$$D = \frac{1}{2}\rho_a U^2 S C_d \qquad (1)$$

where ρ_a = density of air, U = terminal velocity, S = surface area of the particle projection on a plane perpendicular to velocity. In the above equation, the surface area S is an unknown. To remedy this, an equivolumetric diameter D_{eq}, which is the diameter of the sphere with the same volume as that of the particle, is typically referred to in related studies.

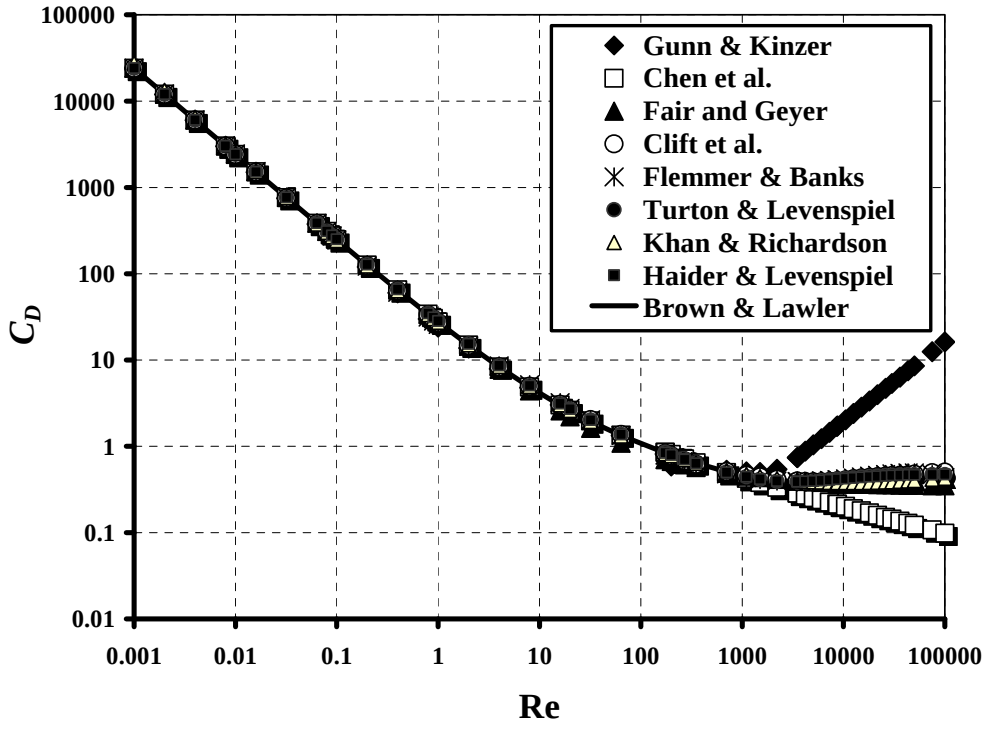

Figure 5: Comparison of sphere drag correlations by various authors.

Brown and Lawler [28] recently re-evaluated the experimental sphere drag data available in literature to account for the effect of walls since much of the data was measured in small diameter cylindrical vessels. They proposed new correlations for the drag coefficient based on corrected experimental data. In the current project, the new sphere drag coefficient correlation based on Eq. (19) of Ref. [28] has been considered since it provides the best fit to the existing experimental data for the entire range of Reynolds number ($10^{-3} \leq$ Re $\leq 3.5\times10^{5}$) considered . The correlation is given by the relation:

$$C_d = \frac{24}{\mathrm{Re}}\left(1+0.150\,\mathrm{Re}^{0.681}\right)+\frac{0.407}{1+\frac{8710}{\mathrm{Re}}} \qquad (2)$$

Since sand particles are non-spherical, drag coefficient correlations for non-spherical particles were also compared for error and range of applicability. Chhabra et al. [29] have critically evaluated the widely-used drag correlations from 19 studies with a resulting data base of 1900 data points for a range of Reynolds number ($10^{-4} \leq \mathrm{Re} \leq 5\times10^{5}$). One of the methods investigated by Chhabra et al. was the Haider and Levenspiel's non-spherical correlation [25]. The Haider and Levenspiel correlation is valid for the particle Reynolds number less than 2.5×10^{5}. The maximum particle Reynolds number observed in this study (for very fine to coarse size particles and a velocity of 40 m/s) was of the order

of 100 to 1500, respectively. Haider and Levenspiel relate the shape of a non-spherical particle by a shape factor ϕ which is defined as the ratio of the surface area of a sphere having the same volume as the particle to the actual surface area of the particle. Thus for non-spherical particles: 0 < ϕ < 1. The sand particle shape factor can vary from 0.3 to as high as 0.9. The drag coefficient correlation of Haider and Levenspiel for non-spherical particles with a shape factor ϕ is given by:

$$C_d = \frac{24}{\mathrm{Re}}\left(1 + b_1\,\mathrm{Re}^{b_2}\right) + \frac{b_3 + \mathrm{Re}}{b_4 + \mathrm{Re}} \tag{3}$$

where

$$\begin{aligned} b_1 &= \exp(2.3288 - 6.4581\phi + 2.4486\phi^2) \\ b_2 &= 0.0964 + 1.5565\phi \\ b_3 &= \exp(4.905 - 13.8944\phi + 18.4222\phi^2 - 10.2599\phi^3) \\ b_4 &= \exp(1.4681 + 12.258\phi - 20.7322\phi^2 + 15.8855\phi^3) \end{aligned} \tag{4}$$

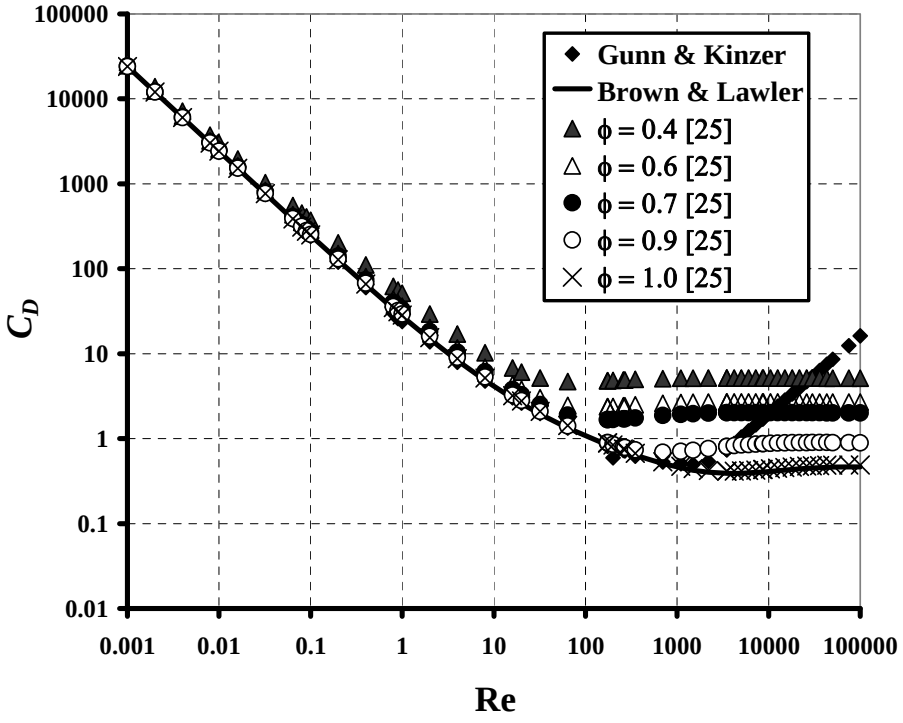

Figure 6: Comparison of non-spherical and spherical particle drag correlations by various authors.

The results of Chhabra et al. [29] indicate that Haider and Levenspiel correlation satisfactorily predicts drag for particle with values of ϕ > 0.67. Figure 6 shows a comparison of the Haider and Levenspiel correlation (for non-spherical particles) prediction with other methods. It is evident from the figure that for small values of shape factor (elongated shape), a significant increase in drag results. As mentioned earlier, the maximum particle Reynolds number observed in this study (for very fine to coarse size particles and a velocity of 40 m/s) was of the order of 100 to 1500, respectively. Based on Fig. 6, non-spherical particle drag can be as high as 6-7 times for a shape factor of ϕ < 0.5. Therefore, in the design of an actual IPS system, the shape factor (or the sphericity) of the sand particle should be given due consideration. In the current study, a shape factor of ϕ = 1 has been considered along with the drag coefficient correlation of Brown and Lawler, Eq. (2) above. In addition, a sand particle density ρ_p = 1422 kg/m^3 has been used.

Another important consideration in design or analysis of IPS systems is the way a sand particle impacts a surface and rebounds. The particle collision with the surface could be treated as elastic or inelastic, however, inelastic collisions have been found to give more accurate scavenge efficiencies. In literature [30–33], the inelastic impacts are characterized by restitution coefficients that are ratios relating the incident and rebound angles (β_1, β_2) and velocities (V_1, V_2) and its components before and after the impact (see Fig. 7). These restitution coefficients are obtained from experiments and are expressed as fourth-degree polynomials that are a function of the particle incident angle β_1. In the present investigation, the restitution coefficients reported by Tabakoff and Hamed [33] for their aluminum target surface have been used and are given by Eq. (5). Figure 8 presents a plot of the restitution coefficients for incident angles between $0 \leq \beta_1 \leq \pi/2$.

$$\frac{V_2}{V_1} = 1 - 2.03\beta_1 + 3.32\beta_1^2 - 2.24\beta_1^3 + 0.472\beta_1^4$$

$$\frac{\beta_2}{\beta_1} = 1 + 0.409\beta_1 - 2.52\beta_1^2 + 2.19\beta_1^3 - 0.531\beta_1^4$$

$$\frac{V_{n2}}{V_{n1}} = 0.993 - 1.76\beta_1 + 1.56\beta_1^2 - 0.49\beta_1^3$$

$$\frac{V_{t2}}{V_{t1}} = 0.988 - 1.66\beta_1 + 2.11\beta_1^2 - 0.67\beta_1^3$$

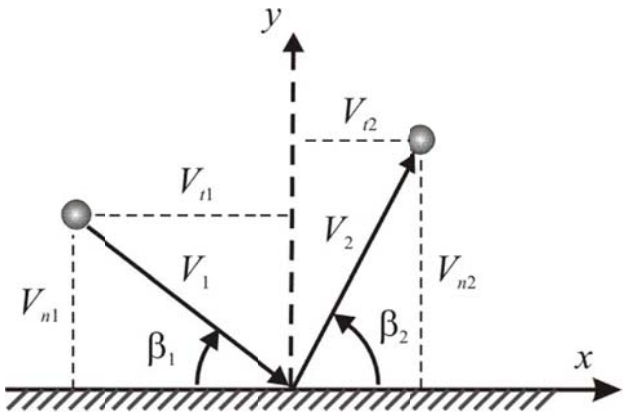

Figure 7: Sand particle impact and rebound geometry.

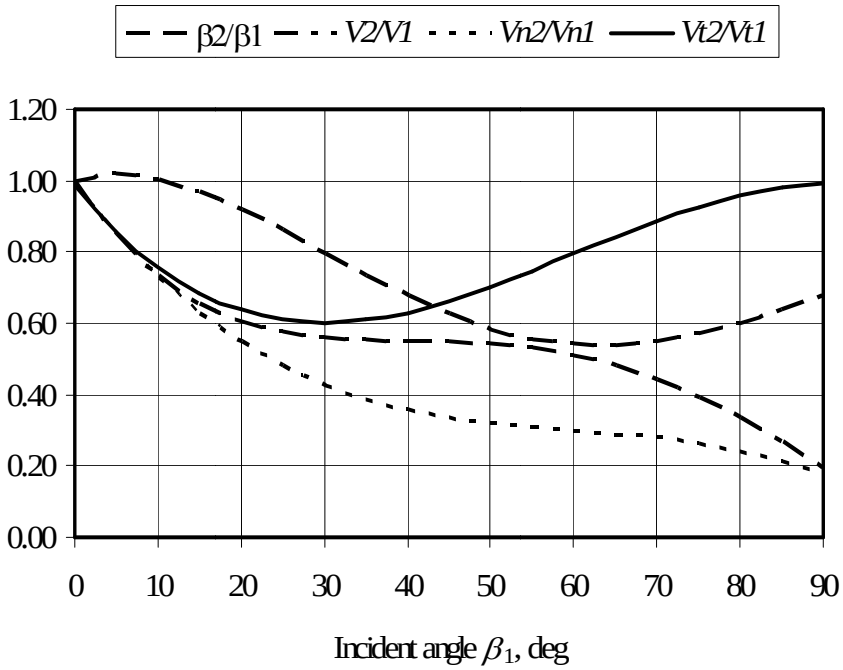

Figure 8: Sand particle angle and velocity restitution ratios versus incident angle on an aluminum wall.

3. Design Methodology

This section presents the details of the new design methodology developed in this investigation. Figure 9 represents an example of a typical IPS system, based on a typical axisymmetric helicopter engine particle separator shown in Fig. 3, represented as a five-element airfoil configuration. A careful examination of Fig. 9 suggests that the path of sand particles can be controlled by giving a specific contour to the surface areas where the particles impact as well as positioning of airfoil elements 1

through 5. Since particle paths are to a great degree influenced by the rebound characteristics, these characteristics could be used to determine the appropriate surface curvature. Thus, the new design method makes use of both the particle inertia as well as rebound characteristics as a means to direct particle paths towards scavenge areas. Since particle flow path as well as rebound characteristics depend on the IPS system geometry, the multi-point inverse airfoil design methodology is employed to obtain the desired geometry through specification of the required flow and rebound characteristics.

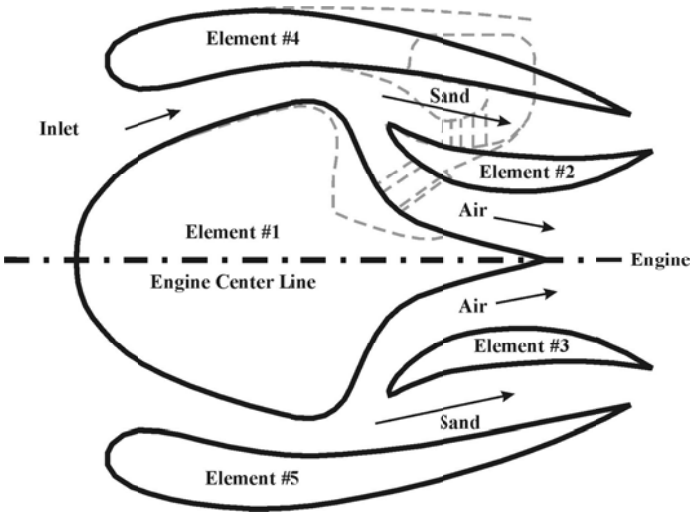

Figure 9: A five-element airfoil configuration model for IPS system.

To facilitate the design, a MATLAB GUI (Graphical User Interface) was developed to carryout analysis or design in an interactive manner. The GUI, shown in Fig. 10, performs four major tasks or functions, namely: (1) synthesis, (2) analysis, (3) the inverse design, and (4) the optimization. The synthesis component defines an initial configuration of a multi-element airfoil based IPS system. This is achieved by generating multiple airfoil geometries and positioning them subject to a set of geometric constraints such as size of the engine and inlet in terms of maximum diameter and length of each airfoil element. The analysis component performs flow and particle trajectory analysis of the multi-element airfoil configuration. The output from the analysis engine is used to simulate particle trajectories through the IPS system. The particle trajectories are initiated sufficiently ahead of the IPS system and terminate either at the exit if they not strike any surface or at the location where they impinge upon any of the airfoil surface. The trajectories are displayed in the GUI after every run through the analysis engine. The inverse design function is used for interactive design of the element geometries once the particle trajectory and impact characteristics have been determined. Finally, the optimization function analyzes the results of analysis engine and shape optimizes the geometry of the IPS system, based on a given objective function and geometric constraints. This is achieved by employing a heuristic optimizer to search for an optimal design within the specified constraints. The following sections describe the above program functions in greater detail.

3.1 The Synthesis Function

As mentioned earlier, the synthesis component defines an initial configuration of a multi-element airfoil based IPS system. The first step in this process is to design individual airfoil geometries that will represent the central hub (element #1 in Fig. 9), the engine housing (elements #2 & #3 in Fig. 9), and the outer engine cowling (elements #4 & #5 in Fig. 9). Taking advantage of symmetry about the engine centerline, only elements #1, #2 and #4 need to be designed since elements #2 and #4 are mirror images of elements #3 and #5, respectively. The design of the individual airfoils is accomplished with the help of PROFOIL, a multipoint inverse airfoil design code [12–15]. The details of which are presented later in this paper. The GUI is used to define initial airfoil geometries and load them into the design space, each airfoil element at a time, by altering the PROFOIL input script to generate the IPS airfoil elements. The designer, afterwards, has the ability to position each element into its appropriate space and generate the multi-element IPS configuration. This positioning ability is accomplished by implementing translational, rotational, and scaling functions. To give the designer more precision while designing, the amount by which the element is positioned can be specified to the level of first decimal point. The synthesis engine deals with a 2-D design space (x, y). To move an airfoil element, spatial increments dx and dy are added to the original coordinates (x, y) of the airfoil to obtain the new coordinates (x', y') as follows:

$$x' = x + dx\,,\; y' = y + dy \tag{6}$$

To rotate an airfoil element, the transformation equations for rotation about a specified rotation position (x_r, y_r) are given by:

$$\begin{aligned} x' &= x_r + (x - x_r)\cos\theta - (y - y_r)\sin\theta \\ y' &= y_r + (x - x_r)\sin\theta + (y - y_r)\cos\theta \end{aligned} \tag{7}$$

where θ is the rotation angle. To rescale an airfoil element, the transformation equations for scaling about a fixed reference point (x_f, y_f) are given by:

$$\begin{aligned} x' &= x_f + (x - x_f)s_x \\ y' &= y_f + (y - y_f)s_y \end{aligned} \tag{8}$$

where s_x and s_y are the scale factors in the x and y directions, respectively. In this study, (x_r, y_r) and (x_f, y_f) are taken to be the trailing edge coordinates of the airfoil element. Moreover, s_x and s_y are taken to be equal to preserve the original airfoil shape.

As mentioned earlier, symmetry about the engine centerline requires that only elements #1, #2 and #4 be designed since element #2 and #4 are mirror images of element #3 and #5, respectively. Thus, once

a design of elements #1, #2 and #4 is obtained, the airfoils are arranged into an IPS system whose geometry is saved in a MATLAB data file for later use. A design box was implemented into the synthesis engine to constrain the element positioning inside the box, were the width and height of the box can be specified by the designer. The synthesis function also has the capability of rendering the IPS system in 3D by revolving each element about the engine centerline axis (Fig..

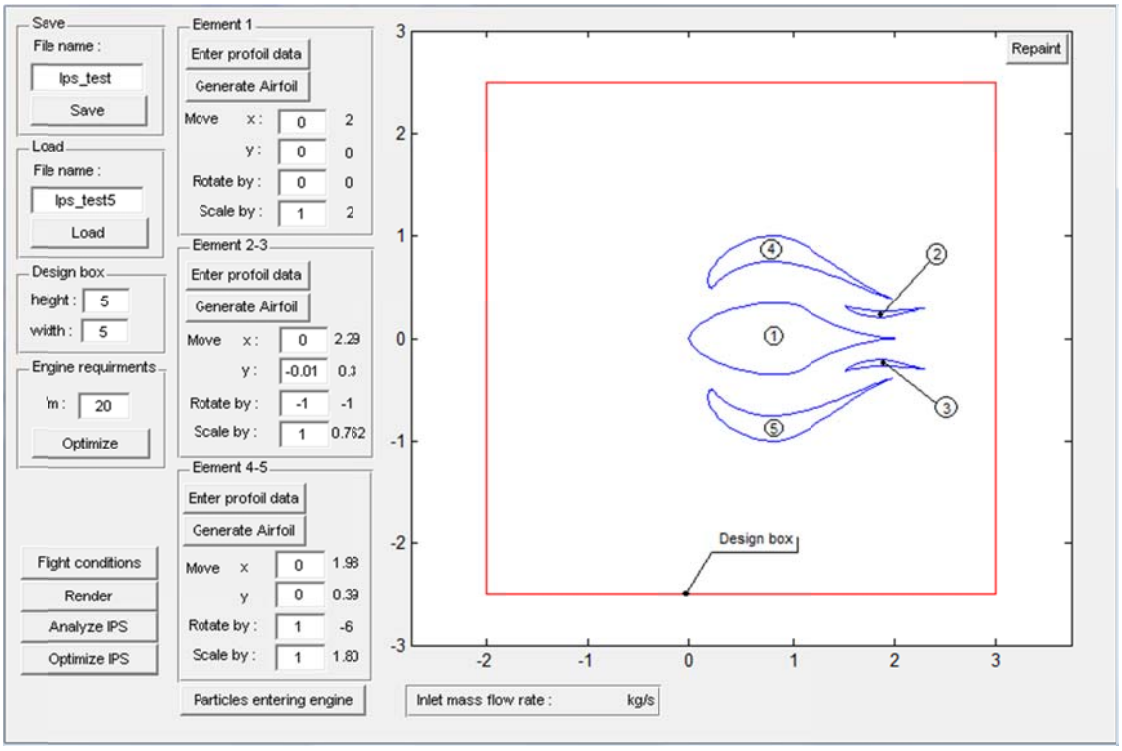

Figure 10: The MATLAB GUI for IPS system design

3.2 The Analysis Function

The analysis function performs flow and trajectory analysis of a multi-element airfoil configuration. The IPS system analyzer is able to perform impingement analysis using spherical/non-spherical solid particles as well as water droplets for a range of Reynolds number ($10^{-4} \le \mathrm{Re} \le 5\times10^{5}$).

The flow analysis code employs the panel method of Hess and Smith [34] which is an inviscid flow analysis method for multi-element configurations. This method determines the velocity potential field around multi-element airfoil configurations.

To determine the sand particle trajectory, a force/momentum balance is applied on a particle moving through air. The resulting momentum equation is integrated starting at known initial conditions until the particle impacts a surface panel or travels past the entire multi-element configuration without impact. Similar studies related to sand and water droplet impingement and ice accretion on aircraft

and engine inlet surfaces are available in literature [35–40]. The same approach has been used in this study. The different forces acting on a particle are based on the body reference system which differs from the wind axis system by the angles of attack. If $\overrightarrow{r_p}$ and $\overrightarrow{V_p}$ represent particle position and velocity vectors with respect to the body reference frame, the particle momentum equation can be written as:

$$m_p \frac{d^2 \overrightarrow{r_p}}{dt^2} = \overrightarrow{F_a} + \overrightarrow{F_g} \tag{9}$$

where m_p is the particle mass, $\overrightarrow{F_a}$ the aerodynamic force (pressure and shear) and $\overrightarrow{F_g}$ the gravity force. The gravity force is related to the weight of the particle as follows:

$$\overrightarrow{F_g} = m_p g(\sin\theta\vec{i} - \cos\theta\vec{k}) = \rho_p V_p g(\sin\theta\vec{i} - \cos\theta\vec{k}) \tag{10}$$

where *g* is the gravitational acceleration. The aerodynamic force is due to the pressure and shear forces acting on the particle surface. If we consider S_p as the particle surface and $\vec{n}$ the normal vector on the particle surface and $\vec{k}_p$ the direction of the local vertical axis, the aerodynamic force can be expressed by the relation:

$$\overrightarrow{F_a} = -\int_{S_p} (p - \rho_a gz)\vec{n}dS + \int_{S_p} \overline{\overline{\tau}} \cdot \vec{n}dS \tag{11}$$

The term relating the gravity force is rewritten as:

$$\rho_a \int_{S_p} gz\vec{n}dS = \rho_a \int_{V_p} \nabla(gz)dV = \rho_a g V_p \vec{k}_p = \rho_a g V_p(-\sin\theta\vec{i} + \cos\theta\vec{k}) \tag{12}$$

where V_p is the particle volume. The others terms of the Eq. (11) can be written in two parts. The first, in the same direction as the velocity $\vec{U}$ (which is the flow velocity in the body reference frame), is the drag, while the second term, in the direction perpendicular to $\vec{U}$, is the lift. Here ρ_a is the density of air, and *p* the ambient pressure. Studies indicate that there is no lift if the particle does not have a rotational movement and keeps an axisymmetric shape along the $\vec{U}$ direction, and if the flow is irrotational. On the basis of this assumption, the lift force can be treated as zero and thus only the drag force needs to be considered. Moreover, because the small size of the particles is in the range where shear forces cannot be neglected, the drag force evaluation needs to consider both pressure and shear forces. Since, such a calculation can be very demanding, a more convenient and commonly used

method is to use some form of empirical correlation for the drag coefficient of particle. As mentioned earlier, in the present investigation, the drag coefficient correlation of Brown and Lawler, Eq. (2), is used to determine the drag force from Eq. (1). Finally, the aerodynamic force is given by the following relation:

$$\overrightarrow{F_a} = \rho_a\, g V_p(-\sin\theta\,\vec{i} + \cos\theta\,\vec{k}) + \frac{1}{2}\rho_a S C_d U\vec{U} \tag{13}$$

Substituting the above expressions for both aerodynamic force and gravity force in the particle momentum equation, Eq. (9), yields:

$$\rho_p V_p \frac{d^2\overrightarrow{r_p}}{dt^2} = (\rho_a - \rho_p) g V_p(-\sin\theta\vec{i} + \cos\theta\vec{k}) + \frac{1}{2}\rho_a S C_d U\vec{U} \tag{14}$$

By assuming that the particle surface area and volume are $S = \pi D_{eq}^2/4$ and $V_p = \pi D_{eq}^3/6$, respectively, and that the Reynolds number based on equivolumetric particle diameter D_{eq} is $\mathrm{Re} = \rho_a D_{eq} U/\mu_a$, the previous equation can be rewritten as

$$\frac{d^2\overrightarrow{r_p}}{dt^2} = \frac{\rho_a - \rho_p}{\rho_p} g(-\sin\theta\vec{i} + \cos\theta\vec{k}) + \frac{3C_d\,\mathrm{Re}\,\mu}{4\rho_p D_{eq}^2}\vec{U} \tag{15}$$

Finally, introducing two parameters $K_g = (\rho_p - \rho_a)g/\rho_p$ and $K_a = \rho_p D_{eq}^2/(18\mu_a)$ in the above equation and noting that $\vec{U} = \overrightarrow{V_a} - \overrightarrow{V_p}$, yields:

$$\frac{d^2\overrightarrow{r_p}}{dt^2} + \frac{C_d\,\mathrm{Re}}{24K_a}\frac{d\overrightarrow{r_p}}{dt} = K_g(\sin\theta\vec{i} - \cos\theta\vec{k}) + \frac{C_d\,\mathrm{Re}}{24K_a}\overrightarrow{V_a} \tag{16}$$

where $\overrightarrow{V_a} = u_a\vec{i} + w_a\vec{k}$. Note that this second-order differential equation is nonlinear because of the term $C_d\,\mathrm{Re}/(24K_a)$, which depends on the particle position and the velocity. The difficulty to determine the term $C_d\,\mathrm{Re}/(24K_a)$ suggests that a numerical technique must be employed to integrate the momentum equation, Eq. (16).

The well-known fourth-order Runge-Kutta method [41] is used to integrate the momentum equation. For this purpose, the momentum equation is written as

$$\frac{d^2\vec{r_p}}{dt^2} + \delta\frac{d\vec{r_p}}{dt} = \vec{\beta} \tag{17}$$

where $\vec{\beta} = (\delta u_a + K_g \sin\theta)\vec{i} + (-K_g \cos\theta + \delta w_a)\vec{k}$ and $\delta(\vec{r_p}, \vec{V_p}) = \frac{C_d \,\mathrm{Re}}{24K_a}$

The above momentum equation, which is a second-order differential equation, can be decomposed into two first-order differential equations:

$$\frac{d\vec{V_p}}{dt} = \vec{\beta} - \delta\vec{V_p} = \vec{f}(\vec{r_p}, \vec{V_p}) \qquad \text{and} \qquad \frac{d\vec{r_p}}{dt} = \vec{V_p} \tag{18}$$

Starting with an initial particle position $\vec{r}_{p,i} = (x_{p,i}, z_{p,i})$ and velocity $\vec{V}_{p,i} = (u_{p,i}, w_{p,i})$, the new postion $\vec{r}_{p,i+1} = (x_{p,i+1}, z_{p,i+1})$ and velocity $\vec{V}_{p,i+1} = (u_{p,i+1}, w_{p,i+1})$ are calculated with the aid of the following relations based on the Runge-Kutta method:

$$\vec{r}_{p,i+1} = \vec{r}_{p,i} + \tau\vec{V}_{p,i} + \frac{\tau}{6}(\vec{k_1} + \vec{k_2} + \vec{k_3}) \tag{19}$$

$$\vec{V}_{p,i+1} = \vec{V}_{p,i} + \frac{1}{6}(\vec{k_1} + 2\vec{k_2} + 2\vec{k_3} + \vec{k_4}) \tag{20}$$

The four coefficients $\vec{k_1}, \vec{k_2}, \vec{k_3}$ and $\vec{k_4}$ in the above equation are given by:

$$\vec{k_1} = \tau\vec{f}(\vec{r}_{p,i}, \vec{V}_{p,i}) \tag{21}$$

$$\vec{k_2} = \tau\vec{f}(\vec{r}_{p,i} + \frac{\tau}{2}\vec{V}_{p,i}, \vec{V}_{p,i} + \frac{1}{2}\vec{k_1}) \tag{22}$$

$$\vec{k_3} = \tau\vec{f}(\vec{r}_{p,i} + \frac{\tau}{2}\vec{V}_{p,i} + \frac{\tau}{4}\vec{k_1}, \vec{V}_{p,i} + \frac{1}{2}\vec{k_2}) \tag{23}$$

$$\vec{k_4} = \tau\vec{f}(\vec{r}_{p,i} + \vec{V}_{p,i} + \frac{\tau}{2}\vec{k_2}, \vec{V}_{p,i} + \vec{k_3}) \tag{24}$$

where τ is the integration time step. This time step must neither be too small to result in a long computation time nor too large that it leads to inaccuracies in computation. A set of initial conditions are required to start the integration. These initial conditions are taken at an upstream point in space

where the flow is unperturbed, that is, the flow velocity at this point must not differ from the free stream $\overrightarrow{V_\infty}$ value by more than 1%. The following relation gives the initial velocity of the particle:

$$\overrightarrow{V_p^0} = \overrightarrow{V_a^0} - \overrightarrow{U^0} \tag{25}$$

With $\overrightarrow{V_a^0}$ the flow velocity in the unperturbed flow, that is $\overrightarrow{V_\infty}$, and $\overrightarrow{U^0}$ the terminal velocity of falling particle. The terminal velocity $\overrightarrow{U^0}$ can be calculated with the relation

$$\frac{C_d \,\mathrm{Re}}{24} U^0 = K_a K_g \tag{26}$$

If we consider particles with an equivolumetric diameter between 10 μm and 80 μm, the Stokes law can be applied and the previous equation becomes $U^0 = K_a K_g$. Consequently, the initial particle velocity is

$$u_p^0 = u_\infty \text{ and } w_p^0 = w_\infty - K_a K_g \tag{27}$$

If the equivolumetric diameter is greater than 80 μm, the previous equation becomes inaccurate and the velocity calculated is greater than the true velocity. By using the calculated velocity in the momentum equation, acceleration results that ultimately leads to the particle terminal velocity.

The particle trajectories are initiated at a distance of about five chord lengths (of the middle airfoil representing the engine centerline) and are calculated until they either impact any of the airfoil elements or go past around it. The location of the particle impingement point on any airfoil element surface is determined using a systematic search approach. While the particle is upstream of any airfoil element, no impact or impingement search is performed. Once the particle reaches the border or the bounding box around any of the elements along the *x*-axis, a search is initiated that checks for any impingement on surface panels of all elements with the knowledge of the particle position (*x*, *z*). This is accomplished as follows. First of all, the particle trajectory is assumed to be a straight line, from the old position (x_i, z_i) to the new position (x_{i+1}, z_{i+1}). Each airfoil element surface is represented by means of a number of flat and straight panels. In order to determine whether an impact has occurred on a panel [represented by the vertices (x_1, z_1) and (x_2, z_2)] or not, the following two conditions are verified:

$$x_{\min} \le x_{i+1} \text{ and } x_i \le x_{\max}, \; z_{\min} \le z_{i+1} \text{ and } z_i \le z_{\max} \tag{28}$$

with $x_{\min} = \min(x_1, x_2)$, $z_{\min} = \min(z_1, z_2)$, $x_{\max} = \max(x_1, x_2)$ and $z_{\max} = \max(z_1, z_2)$. When all of the above conditions are satisfied for a panel, the impact takes place on that panel. The location of the impact point is calculated by considering the particle trajectory parametric equations given by:

$$\begin{aligned} x_{i+1} &= x_i + t_0(x_{i+1} - x_i) = x_i + t_0 l_0 \\ z_{i+1} &= z_i + t_0(z_{i+1} - z_i) = z_i + t_0 n_0 \end{aligned} \tag{29}$$

where (l_0, n_0) is the trajectory direction vector and t_0 is the parameter related to that trajectory. All points that belong to the trajectory corresponding to the impingement or impact must satisfy $0 \le t_0 \le 1$. Similarly, the parametric equations for each panel are:

$$\begin{aligned} x &= x_2 + t_1(x_1 - x_2) = x_2 + t_1 l_1 \\ z &= z_2 + t_1(z_1 - z_2) = z_3 + t_1 n_1 \end{aligned} \tag{30}$$

And all points located on the panel must satisfy the additional condition: $0 \le t_1 \le 1$. Hence, the two parameters t_0, t_1 determine whether the particle trajectory intercepts a surface panel or not. Numerically, t_0 is calculated first and checked to see if it satisfies the condition $0 \le t_0 \le 1$. If this condition is satisfied, only then t_1 is calculated to verify whether there is any impact on the panel. The coordinates of the impact point are found from t_0 and (l_0, n_0).

Once an impact has been located, the particle incident angle β_1 with respect to the panel along with its velocity components (V_1, V_{n1}, V_{t1}) are calculated. The rebound angle β_2 and velocities (V_2, V_{n2}, V_{t2}) are then determined from the restitution ratios given by Eq. (5). The new particle location is determined after impact and rebound from where once again the particle momentum equation is used to track particle after impact. This step is repeated after each impact till the particle crosses a pre-selected location along the axial direction, typically past the entrance to the engine core flow which in the present investigation is fixed at the trailing edge location of the outer elements #4 and #5. The entire trajectory, impact and rebound procedure is repeated for each sand particle released in the flow from different upstream locations (y_0) along the y-axis while keeping a constant upstream distance of five chord lengths ($x_0 = -5c$). Thus, the impingement regions on individual elements are determined by an appropriate sweep of the y-axis.

3.3 The Multi-Point Inverse Design Function

The inverse design function is used for interactive design of the element geometries. The first step in this process is to design individual airfoil geometries of: (a) central hub, element #1 in Fig. 9, (b) the engine core, elements #2 & #3 in Fig. 9, and (c) the engine nacelle, elements #4 & #5 in Fig. 9. Taking advantage of symmetry about the engine centerline axis, only elements #1, #2 and #4 are designed since elements #2 and #4 are mirror images of elements #3 and #5, respectively. As mentioned earlier,

the design of the individual airfoils is accomplished with the help of PROFOIL, a multipoint inverse airfoil design code [15]. The GUI is used to define initial airfoil geometries and load them into the design space, one airfoil element at a time, by altering the PROFOIL input script for that element. The designer, afterwards, has the ability to position each element into its appropriate space and generate the multi-element IPS configuration. Since the multi-point inverse design method plays a key role in the design of the IPS geometry, details of the method are presented next.

3.3.1 The PROFOIL Code

PROFOIL [15] is a low speed airfoil design code. It employs the inverse design approach as opposed to the direct design approach. In the direct design approach (Fig. 11), the airfoil shape is specified first and then analyzed to determine a desired analysis property such as velocity distribution, lift or drag. Here the airfoil shape is adjusted until the desired analysis property is obtained. A drawback of the direct approach is that the designer spends a great deal of time going through a hit-and-trial process of defining different airfoil shapes to achieve the desired analysis property.

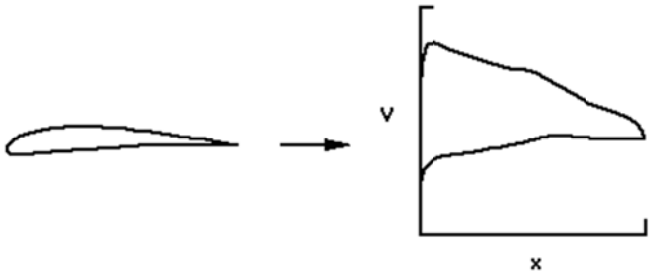

Figure 11: Direct approach to airfoil design [15]

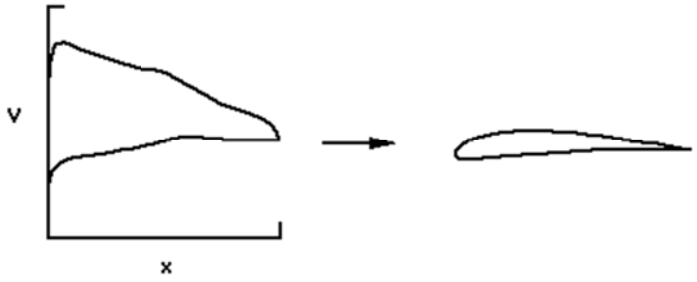

Figure 12: Inverse approach to airfoil design [15]

An inverse airfoil design technique is one in which the airfoil geometry is obtained from a specification of desired velocity distribution(s) (Fig. 12) subject to certain constraints. The method is based on

conformal mapping of flow around a circle (known) to that around the airfoil (desired) through conformal transformation. The method was first proposed by Eppler [12] and later extended to include multi-point design by Selig and Maughmer [13], and further by Saeed and Selig [14] to include design of slot-suction airfoils. The basis of the inverse airfoil design technique stems from the fact that the flow around an arbitrary airfoil may be mapped to the flow about a circle. Since the flow about the circle is easily determined, it remains only to find the transformation or the mapping. Moreover, since the mapping follows the flow or more specifically the velocity distribution, the objective in an inverse design problem is to determine the mapping from the specified airfoil velocity distribution and not from the airfoil shape. Furthermore, since the mapping derivative directly relates to the velocity distribution, it is more convenient to find the mapping derivative instead of the mapping itself. Once the mapping derivative is known, the airfoil shape is then easily determined. In the following section, the basic theory of the generalized multi-point inverse airfoil design technique is briefly described.

Consider the flow about the unit circle centered at the origin in the ζ-plane that is mapped to the flow around an arbitrary airfoil in the z-plane via $z = z(\zeta)$, see Fig. 13. The complex potential for uniform flow of unit velocity at an angle of attack α about the unit circle is then given by

$$F(\varsigma) = e^{-i\alpha}\varsigma + \frac{e^{i\alpha}}{\varsigma} + \frac{i\Gamma}{2\pi}\ln\varsigma \qquad (31)$$

where $\Gamma = 4\pi \sin\alpha$ is the circulation strength required to satisfy the Kutta condition by fixing the rear stagnation point at $\zeta = 1$. The front stagnation point is at $\varsigma = e^{i\phi_s}$ where $\phi_s = \pi + 2\alpha$.

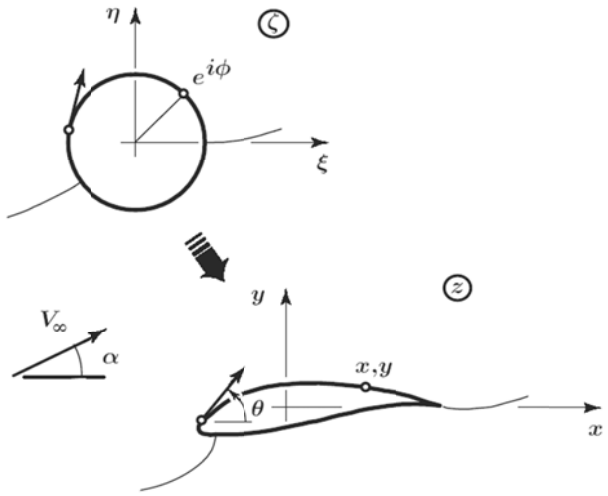

Figure 13: Mapping from circle to airfoil plane.

And the complex velocity is given by

$$\frac{dF}{d\varsigma}=\left(1-\frac{1}{\varsigma}\right)\left(1-\frac{e^{i\phi_s}}{\varsigma}\right)e^{-i\alpha} \tag{32}$$

which on the circle $\varsigma=e^{i\phi}$ becomes

$$\left.\frac{dF}{d\varsigma}\right|_{\varsigma=e^{i\phi}}=4\sin\left(\frac{\phi}{2}\right)\cos\left(\frac{\phi}{2}-\alpha^*(\phi)\right)e^{-i\left(\phi-\pi/2-\pi^*(\phi)\right)} \tag{33}$$

where

$$\pi^*(\phi)=\begin{cases}0, & 0\le\phi\le\pi+2\alpha^*(\phi)\\ \pi, & \pi+2\alpha^*(\phi)\le\phi\le 2\pi\end{cases} \tag{34}$$

Here $\alpha^*(\phi)$ is the design angle of attack for a single-point design. For multi-point design, $\alpha^*(\phi)$ can be considered as a piecewise function, i.e., a constant design angle of attack could be used for each segment on the airfoil thereby allowing a distribution of angles of attack specifications along different segments. Since the velocity distribution corresponds to the lift coefficient which in turn depends on the angle of attack, the velocity distribution along different airfoil segments can be related to different angle of attack conditions, i.e., $\alpha^*(\phi)$ or $C_l^*(\phi)$. A good approximation is given by $C_l^*(\phi) = 2\pi(1+0.78t/c)\sin\alpha^*(\phi)$, where t/c is the airfoil thickness-to-chord ratio and $\alpha^*(\phi)$ corresponds to the zero-lift line. The resulting airfoil will, therefore, exhibit the design characteristics (velocity distribution $v^*(\phi)$ and $C_l^*(\phi)$) when operated at the corresponding $\alpha^*(\phi)$. Typically, good performance is required over a range of angles of attack. For example, high-lift (high angle of attack) performance may be required as well as low-lift (low angle of attack). Thus, for instance, upper surface velocity distribution can be prescribed for a high angle of attack while simultaneously lower surface velocity distribution can be prescribed for a low angle of attack. This multi-point inverse design process is illustrated in Fig. 14 where A, B and C correspond to multiple design requirements based on, for example, the different flight segments of an aircraft.

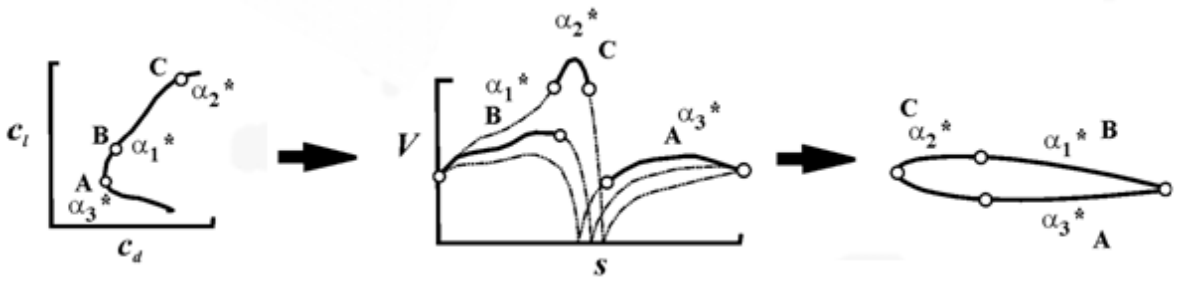

Figure 14: The multi-point inverse airfoil design process.

The derivative of the mapping function on the unit circle is assumed to be of the form

$$\frac{dz}{d\varsigma} = \left(1 - e^{-i\phi}\right) \exp \sum_{m=0}^{\infty} (a_m + ib_m) e^{1-\varepsilon} = (a_m + ib_m) e^{1-\varepsilon}\, \mathrm{e}^{P(\phi)+iQ(\phi)} \tag{35}$$

which must satisfy three conditions: the airfoil trailing-edge angle must be finite, the flow at infinity must be unaltered, and the airfoil contour must close. These conditions on the mapping lead to the integral constraints [12, 13] that must be satisfied for multipoint inverse airfoil design. Here ε is the finite trailing edge angle.

The complex velocity in the *z*-plane on the boundary of the airfoil is expressed as

$$\left.\frac{dz}{d\varsigma}\right|_{\varsigma = e^{i\phi}} = v^{*}(\phi) e^{-i\theta^{*}(\phi)} \tag{36}$$

To relate $v^{*}(\phi)$ and $\theta^{*}(\phi)$ to the series coefficient of the mapping derivative, the complex velocity is written alternatively as

$$\left.\frac{dF}{d\varsigma}\right|_{\varsigma = e^{i\phi}} = \frac{\left(\dfrac{dF}{d\varsigma}\right)_{\varsigma = e^{i\phi}}}{\left(\dfrac{dz}{d\varsigma}\right)_{\varsigma = e^{i\phi}}} \tag{37}$$

Substituting Eqs. (33), (35) and (36) into Eq. (37) and taking the natural logarithm of the resulting equation yields the following results

$$P(\phi) = -\ln\left\{\frac{(2\sin\phi/2)^{-\varepsilon} v^{*}(\phi)}{2\left|\cos(\phi/2 - \alpha^{*}(\phi)\right|}\right\}; \quad Q(\phi) = \theta^{*}(\phi) + \pi^{*}(\phi) + \varepsilon(\pi/2 - \phi/2) \tag{38}$$

where $0 \le \phi \le 2\pi$. Thus, the specification of velocity $v^{*}(\phi)$ and the angle of attack $\alpha^{*}(\phi)$ uniquely determines $P(\phi)$. Alternatively, specifying the airfoil flow direction $\theta^{*}(\phi)$ and $\pi^{*}(\phi)$, uniquely determines $Q(\phi)$. Since $P(\phi)$ and $Q(\phi)$ are conjugate harmonic functions, then from either one the corresponding harmonic function is determined through the Poisson's integral formula exterior to the circle. Once $P(\phi)$ and $Q(\phi)$ are known, the airfoil coordinates $x(\phi)$ and $y(\phi)$ are then obtained through quadrature.

3.3.2 Multipoint Design Capability of the Theory

The function $P(\phi)$ depends only on ϕ and is defined by specifying velocity distribution $v^*(\phi)$ and the angle of attack distribution $\alpha^*(\phi)$, now called the design velocity and the corresponding design angle of attack distributions, respectively. Since it is only necessary that $P(\phi)$ be continuous, a discontinuity in any one or a combination of the design variables, i.e., $v^*(\phi)$ and $\alpha^*(\phi)$, must be compensated by a corresponding discontinuity in any one or a combination of the remaining design variables. This is the most important point of the theory, and it is on this basis that the multipoint design is accomplished. Thus, the airfoil can be divided into a number of segments along which the design velocity distribution along with the design values for $\alpha^*(\phi)$ are specified. It is helpful for design purposes to let $\alpha^*(\phi)$ be constant over any given segment; whereas, $v^*(\phi)$ should be allowed to vary in order to obtain some desired velocity distribution. Then, in order to ensure continuity between segments, the following condition must be satisfied.

$$P_+(\phi_i) = P_-(\phi_i) \tag{39}$$

or from Eq. (38),

$$\frac{v^*_-(\phi_i)}{\left|\cos(\phi_i/2 - \alpha^*_-(\phi_i)\right|} = \frac{v^*_+(\phi_i)}{\left|\cos(\phi_i/2 - \alpha^*_+(\phi_i)\right|} \tag{40}$$

where ϕ_i is the arc limit between segments i and $i + 1$. For a five-segment airfoil, Eq. (40) will result into four relations that are commonly referred to as continuity constraints. The continuity constraints must be satisfied at the junction of the segments except at the trailing edge. Thus, different design parameters [e.g., angle of attack distribution $\alpha^*(\phi)$] may be specified with respect to different segments on the circle yielding a multipoint design.

The specification of the velocity is not completely arbitrary and must satisfy certain integral constraints that arise due to the conditions on the mapping. These constraints come from the requirement on the mapping that the airfoil trailing edge must be closed and the velocity in the far-field must approach the free stream value. These conditions are commonly referred to as integral constraints and are mathematically expressed as:

$$\oint_{C_z} dz = \oint_{C_\varsigma} \frac{dz}{d\varsigma} d\varsigma = 0; \lim_{\varsigma \to \infty} \frac{dz}{d\varsigma} = 1 \tag{41}$$

where C_z and C_ς are contours about the airfoil and circle, respectively. Thus, application of the constraints to Eq. (35) suggests that the integral constrains are satisfied if and only if

$$a_0 = \frac{1}{2\pi}\int_0^{2\pi} P(\phi)d\phi \qquad = 0$$

$$a_1 = \frac{1}{\pi}\int_0^{2\pi} P(\phi)\cos\phi d\phi = 1-\varepsilon \qquad (42)$$

$$b_1 = \frac{1}{\pi}\int_0^{2\pi} P(\phi)\sin\phi d\phi = 0$$

The satisfaction of these constraint leads to a system of (*N*+3) equations where *N* is the number of segments. As mentioned earlier, the specification of the velocity distributions is not completely arbitrary. It must contain an equal number of unknowns (*N*+3) to obtain a solution of the problem. Typically these unknowns are the velocity levels on (*N*-1) segments, and the remaining 4 variables define the form of the recovery and closure functions for flow at the trailing edge along the upper and lower surfaces. Additional constraints (dependent variables) such as pitching moment, maximum thickness, camber, etc., can also be imposed and satisfied through an iterative procedure by varying some independent variables in the design. Simultaneous solution of the constraints requires a multi-dimensional Newton iteration scheme and is accomplished within 10-15 iterations. Details of the mathematical formulation and various applications of the method are described in Ref. [12-15].

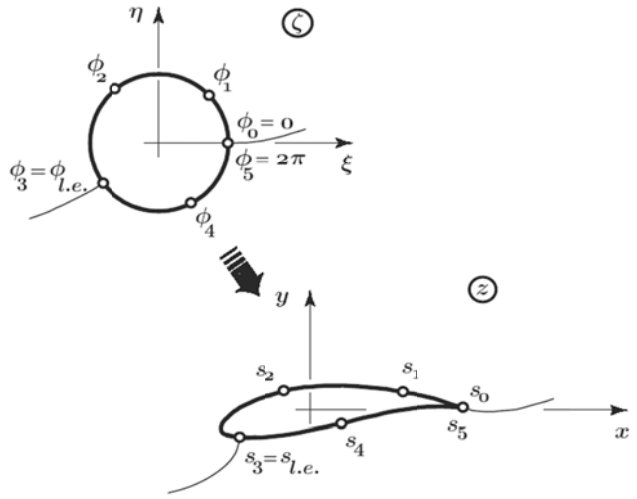

Figure 15: Circle divided into five segments and mapped to a five-segment airfoil.

3.3.3 Numerical Implementation

Consider the mapping shown in Fig. 15 where a circle is divided into five segments and mapped to a five-segment airfoil. The three integral constraints on the mapping Eq. (42) require that three free parameters must be introduced to satisfy these constraints. These free parameters arise from the form of pressure recovery function used in the analysis. In addition, to satisfy the four continuity constraints

Eq. (40) at the junction of the segments (s_1 through s_4 in Fig. 15), another five free parameter must be introduced to obtain a solution. These five parameters are the velocity levels at the junctions based on the desired velocity distribution $v^*(\phi)$ along each segment. Typically, only the first velocity level is specified and the rest are obtained from the four continuity constraints. Practically any desired airfoil property such as camber, thickness and pitching moment coefficient can be incorporated into the inverse design system with iteration on some inverse design parameter. For example, the pitching moment at a given angle of attack may be specified by adjusting the first velocity level.

3.3.4 Linking the Synthesis and Analysis Functions

The analysis function is linked to the synthesis function via the program GUI. In the GUI, two controls namely: (a) Flight conditions and (b) Analyze IPS are included that as their name implies facilitate the task of specifying the flight and ambient conditions, and performing the analysis, respectively. The analysis engine outputs particle trajectory data which is then displayed in the GUI design box (Fig. 16). Figure 17 shows a 3D rendering of the IPS system along with particle trajectories after an analysis run.

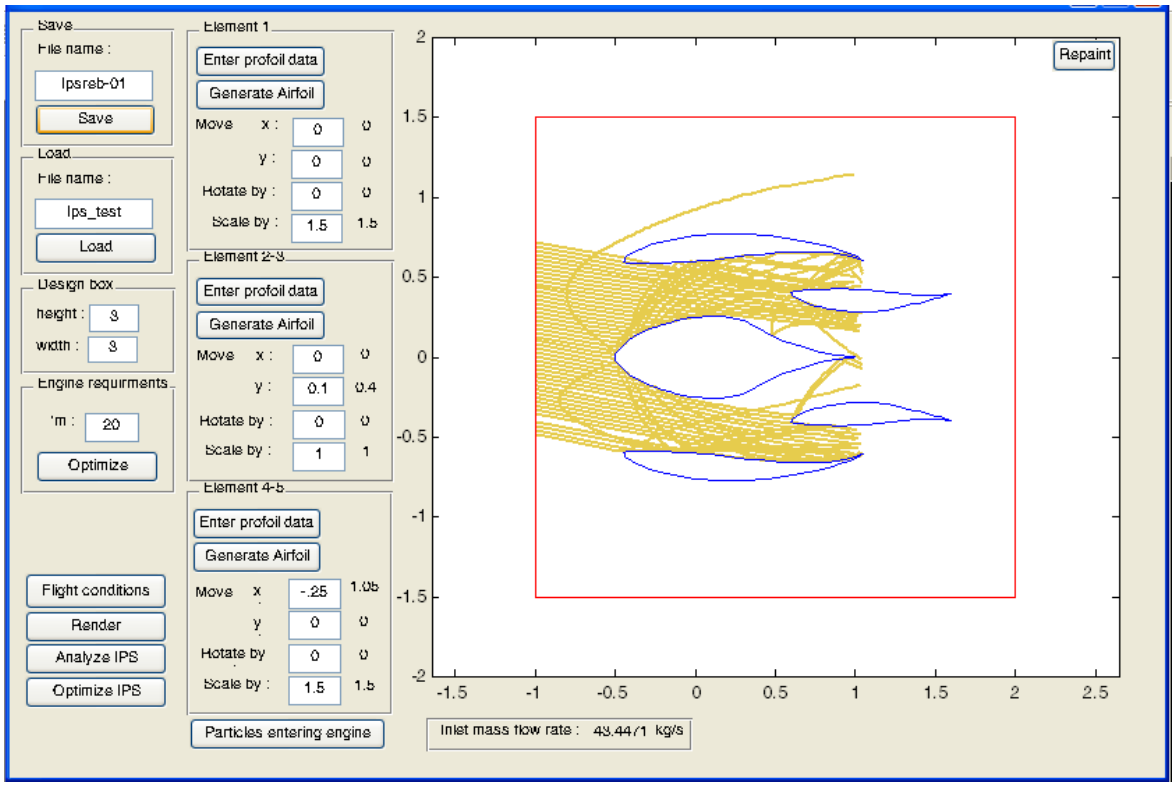

Figure 16: GUI showing IPS system and particle trajectories after an analysis run.

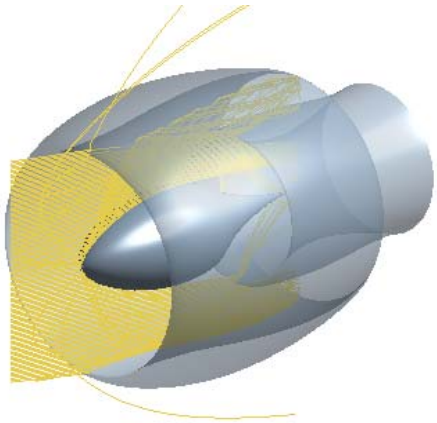

Figure 17: A 3D rendering of the IPS system showing particle trajectories

3.4 The Optimization Function

3.4.1 The Objective Function and Design Constraints

To carry out the optimization of the IPS system, an appropriate objective function must be defined along with the constraints. The objective function chosen in this study is the engine inlet mass flow rate. The constraints could be in the form of operational conditions and geometric shape. Additional constraints such as engine or inlet diameter, length of the various elements, etc. could also be specified to achieve realistic IPS profiles. In this case, the design problem would be to determine the geometry of the IPS system which satisfies the objective function along with the specified constraints. The design would then be achieved by an appropriate inverse design, orientation and scaling of the airfoil elements. The design (shape or profile) of individual elements could in turn be controlled by a specific choice of airfoil camber, thickness, and/or airfoil pitching moment, i.e. airfoil shape parameters.

Hence, the optimization problem at hand involves a vast number of variables that all need to be linked to the objective function and simultaneously accounted for. To accomplish this task, a multi-variable optimization scheme is adopted. The airfoil positioning (translation, orientation and scaling) and airfoil shape parameters (airfoil camber, thickness, and/or airfoil pitching moment) are communicated by the synthesis function to the optimization function to evaluate the objective function. A new IPS geometry is obtained after each design iteration. To optimize the IPS design for given operational conditions and a given engine requirement mass flow rate, the output of the objective function must be minimized to zero. The objective function's general algorithm is given below in Fig. 18.

```
function objective = ips_ObjFun(X)
change positioning property 1 by (X(1))
…….
```

```
change positioning property n by (X(n))
change element shape property 1 to (X(n+1))
……....
change element shape property m to (X( n+m))
if geometry constraints are met
    Analyze IPS and output the mass flow rate
    if the mass flow rate requirement and trajectory analysis limitations are met
        objective= ips_inlet
    else
         objective=penalty
    end
else
    objective= penalty
end
change positioning property 1 by (-X(1))
…….
change positioning property n by (-X(n))
```

Figure 18: The objective function algorithm.

3.4.2 The Optimizer

After implementing an appropriate objective function, the next step was to choose a suitable optimization method. This method should have the ability to search the design space and minimize the given objective function. Since the objective function is non-linear and non-continuous and contains non-linear constraints, the design space needs to be searched in a random manner so that it would not get locked to a local minimum. Such traits are found in heuristic or constrained direct search methods [42] since these methods do not require any information about the gradient of the objective function. In contrast to the more traditional optimization methods that use information about the gradient or higher derivatives to search for an optimal point, direct search method searches a set of points around the current point, looking for one where the value of the objective function is lower than the value at the current point. The direct search method can be used to solve problems for which the objective function is not differentiable, stochastic, or even continuous.

In MATLAB, the direct search method is implemented in a generalized pattern search algorithm or function in conjunction with the Genetic Algorithm toolbox. This method or function is known as Pattern Search function and was chosen was chosen to optimize the IPS design [43]. In the problem at hand, non-linear constraints are present, which are not supplied by the current version of the toolbox, which is why these constraints (the mass flow rate constraint in this case) were implemented inside the objective function as penalties if not satisfied.

The optimizer requires an initial guess (initial design) which is close to or inside the feasible region so that it would converge and would not get locked into a local minimum. To solve this problem, an additional program function is used which gives the designer the ability to optimize only for the inlet

mass flow rate required. Use of this function has been found to yield a good initial design. The function moves elements #2 and #3 in the *y*-direction, changing the inlet area, and analyzes the IPS for the inlet mass flow rate and results in a design with an inlet mass flow rate very close to the one required by the engine.

Results and Discussion

This section presents some of the results on both analysis and design of IPS system. The analysis examples are shown first followed by a few design examples. The examples were performed on a computer with a 3 gigahertz Intel Core 2 Extreme 6800, with a 2 gigabyte 800 MHz ram. In all the problems, the angle of attack was kept at 0 deg and the free stream velocity was set to 40 m/s. The type of sand particles was set either to very fine or medium.

4.1 Analysis Examples

Figure 19 shows comparison of analysis example in which medium sand particles were allowed to (a) impact only without rebound, and (b) rebound after impact. As evident from the figure, the rebounding particle may easily find their way into the core flow of the engine and hence consideration of rebound characteristics is important for both analysis and design of IPS system. The new analysis routine has also been improved to consider only those particles that enter the engine between elements #1 and #4 or #5.

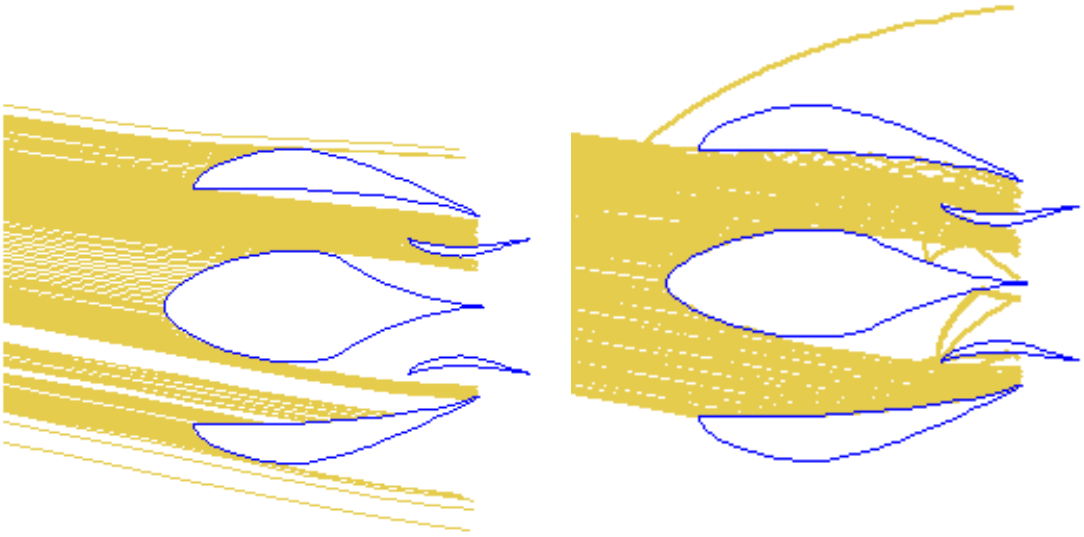

(a) **(b)**

Figure 19: Comparison of particle trajectories: (a) Without rebound, (b) With rebound.

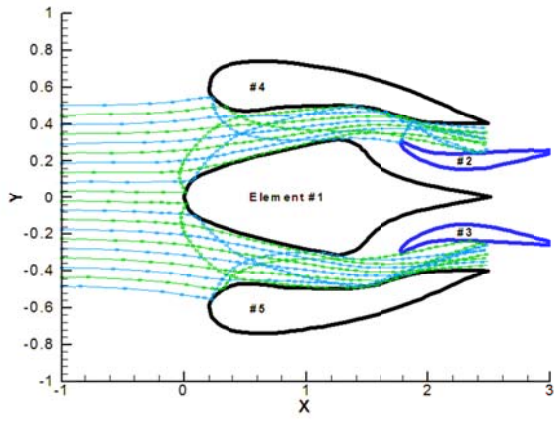

(a)

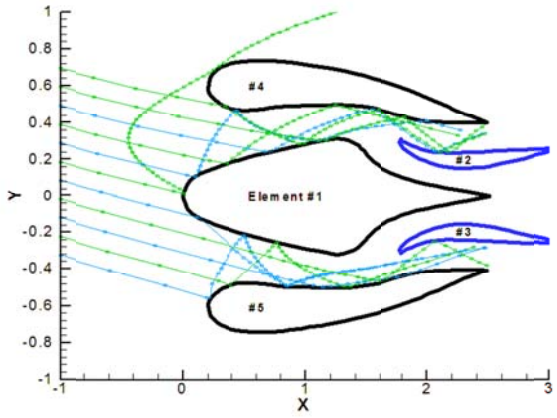

(b)

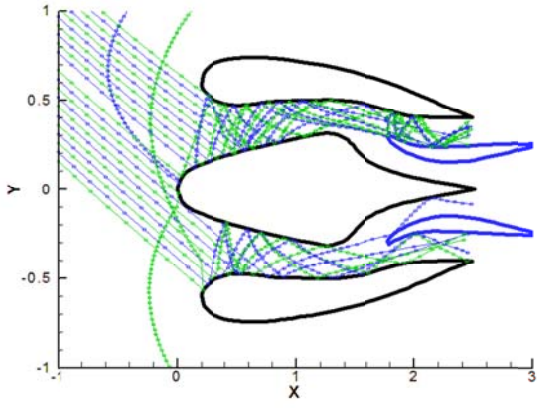

(c)

Figure 20: Sand particle trajectories for (a) Fine, (b) Medium, and (c) Coarse sand.

Figure 20 shows sand particle trajectories for three different particle sizes, namely: (a) fine, (b) medium, and (c) coarse sand. For the IPS configuration shown in the figure, the coarse sand seems likely to enter the engine core. However, the cases reported by Saudi Aramco Aviation suggest fine sand to be the root cause of erosion in turbo-machinery.

4.2 Design Examples

4.2.1 Example 1: A Three-Variable Optimization Case

In this example, three variables were optimized, and were given upper and lower bounds as shown in Table 1. Figure 21(a) shows the un-optimized design in which sand particle trajectories are entering the engine core flow in between elements #1 and #2. The mass flow rate of the un-optimized design is 45 kg/s and the un-optimized design variable values are given in Table 1. The mass flow rate engine requirement was set to a value of 43 kg/s.

In this example, the thickness to chord ratio of element #1 was mainly used to offset the sand trajectories and directing them away from the engine core flow. The computational time for the optimization run was 25 minutes. Figure 21(b) shows the optimized IPS design. The engine core flow is free of sand particles and that the particle trajectories stay clear of the engine core. The mass flow rate of the optimized design is 42.95 kg/s which are close to the required mass flow rate. The optimized design variable values are given in Table 1.

Table 1: Three-variable optimization constraints and results

Element #	Variable #	Shape property	Lower bound	Upper bound	Un-optimized	Optimized
1	1	Thickness	20%	45%	25%	45%
2,3	2	movement in x direction	-0.2	0.5	0	0
	3	movement in y direction	-0.1	0.5	0	-0.05
Objective function		**mass flow rate (kg/s)**	43	-	45	42.95

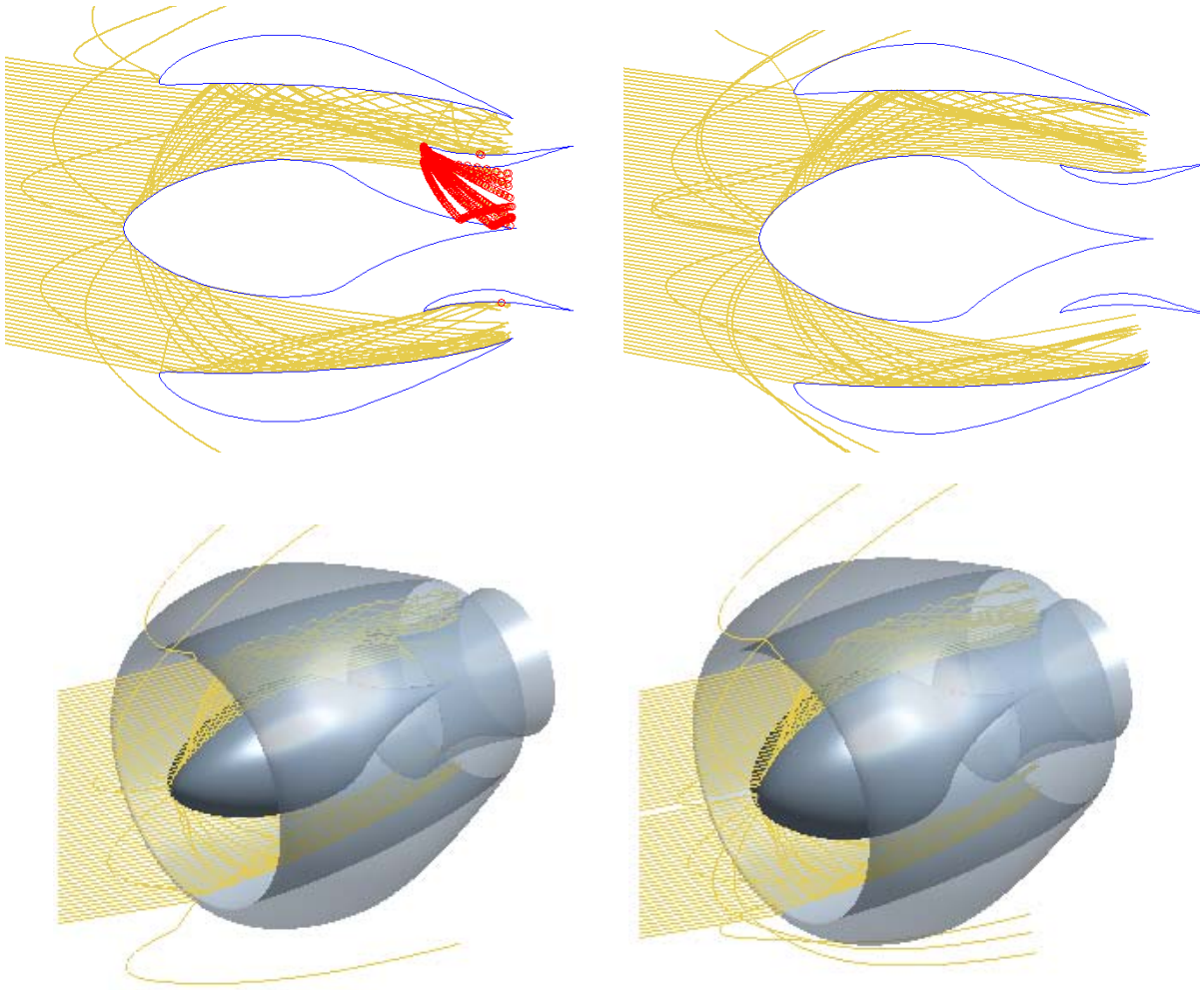

(a) **(b)**

Figure 21: Three-variable optimization example: a) Un-optimized case. b) Optimized case

5.2.2 Example 2: A Nine-Variable Optimization Case

In this example, 9 variables were optimized, and were given upper and lower bounds as shown in Table 2. Figure 22(a) shows the un-optimized design, in which sand particle trajectories are hitting the lower surface of element #2 and the upper surface of element #3 as they enter inside the engine. The mass flow rate of the un-optimized design is 6.776 kg/s and the un-optimized design variable values are given in Table 2. The mass flow rate engine requirement was set to 5.5 kg/s.

The computational time for the optimization run was three hours and thirty minutes. After optimization, the objective function was minimized to zero. Figure 22(b) shows the optimized IPS design. A close-up view of element #2 of the optimized design (Fig. 22) shows clearly that the particle trajectories clear the engine inlet and only hit the upper surface of element #2. The mass flow rate of

the optimized design is 5.5 kg/s which is the required mass flow rate. The optimized design variable values are given in Table 2.

Table 2: Nine-variable optimization constraints and results

Element #	Variable #	Shape property	Lower bound	Upper bound	Un-optimized	Optimized
1	1	Thickness	20%	35%	34%	34.063%
2,3	2	Camber	5%	15%	10%	5%
	3	Thickness	8%	20%	8%	14.25%
	4	Pitching moment coefficient	-0.3	-0.1	-0.18	-0.18
	5	move in x direction	-0.2	0.5	0	-0.063
	6	move in y direction	-0.1	0.5	0	-0.016
4,5	7	Camber	5%	10%	6.8%	6.875%
	8	Thickness	10%	20%	10.8%	10.875%
	9	Pitching moment coefficient	-0.35	-0.2	-0.31	-0.3125
Objective function		**mass flow rate (kg/s)**	4	10	6.776	5.5

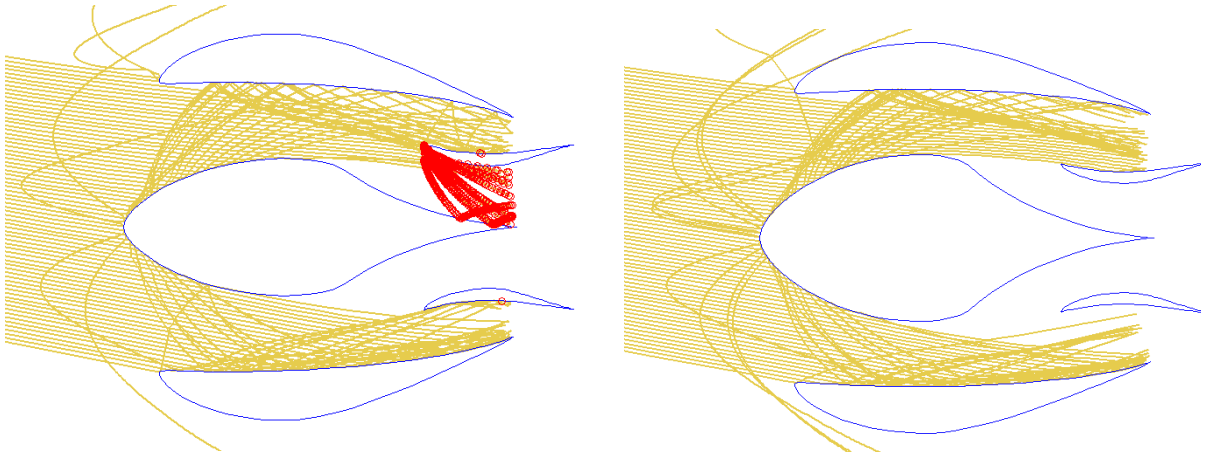

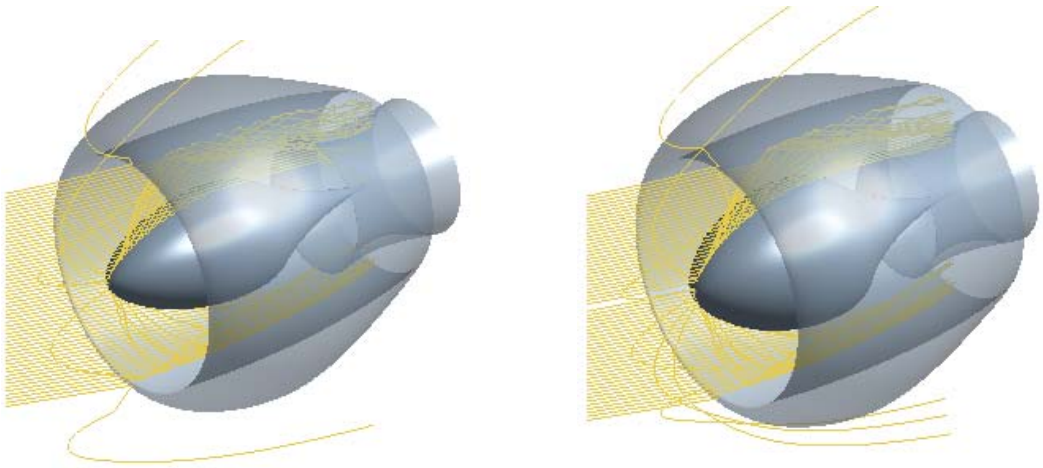

(a) **(b)**

Figure 21: Nine-variable optimization example: a) Un-optimized case. b) Optimized case

Conclusions

Several important conclusions can be drawn from the present investigation.

a. A new and versatile method for the design of an IPS system is now available.
b. Details of development of the efficient design method for aircraft engine sand separator systems are presented along with the methodology used to achieve practical designs of an IPS system.
c. The design method makes use of state-of-the-art and practical design and analysis techniques, such as the inverse aerodynamic design methodology that also takes into account viscous effects to aid in the design of specific profile shapes for engine air intakes. The sand separator design is achieved by giving a specific contour to the intake profile (such as a highly curved bend in the duct) that the contaminants because of their inertial momentum are forced away from the central flow.
d. Since the sand particles can rebound of the air intake walls and enter the engine, the method takes into account sand particle rebound or restitution characteristics in the design.
e. The overall design is accomplished with the aid of optimization techniques in both the inverse aerodynamic design as well as in the sand separator system design.
f. In addition, to facilitate the design, several numerical programs and graphical user interface have been developed to aid in the design and analysis of aircraft engine sand separator systems in an interactive manner.
g. The method has the capability to: 1) Design individual airfoil elements, 2) Orient and arrange airfoils to form a multi-element airfoil based IPS system by employing translational, scaling and rotational functions, 3) Carryout 2D flow and trajectory analysis of multi-element airfoil based

IPS system including impact and rebound off surfaces, and 4) perform design optimization using pattern search – a genetic algorithm based optimization technique.

h. The design of individual airfoils is achieved through the use of the PROFOIL code, a state-of-the-art multi-point inverse airfoil design program. Multiple airfoils are arranged to form a multi-element airfoil based IPS system subject to geometric constraints.
i. A multi-element airfoil flow analysis capability has been developed and used for particle trajectory analysis component of the program.
j. For the optimization component of the program, a computational objective function was successfully implemented and coupled with a pattern search optimizer located in the Genetic Algorithm and Direct Search toolbox in MATLAB. Design and optimization was achieved using multi-variable optimization.
k. Two design examples are presented to illustrate and demonstrate the design method.
l. The study paves way for incorporating erosion in the design in a follow-up project.

Acknowledgement

The author(s) acknowledge the support provided by King Abdulaziz City for Science and Technology (KACST) through the National Science & Technology Unit at King Fahd University of Petroleum & Minerals (KFUPM) for funding this work under project # 08-SPA49-4 as part of the National Science, Technology and Innovation Plan

References

[1] Tabakoff, W., and Hamed, A., "Installed Engine Performance in Dust Laden Atmosphere," AIAA Paper 1984-2488, 1984.

[2] van der Walt, J. P., and Nurick, A., "Prediction of Helicopter Engines Fitted with Dust Filters," *AIAA Journal of Aircraft*, Vol. 23, No. 1, Jan.—Feb. 1995, pp.118-123.

[3] Mann, D., "Case Studies in TRIZ: Helicopter Engine Particle Separator," *The TRIZ Journal* [online], Feb. 1999, http://www.triz-journal.com/archives/1999/02/a/index.htm (retrieved 10 April 2010).

[4] J. Tariq, "Operating Aircraft in Gulf Environment," presented at the Regional Aviation Symposium organized by Saudi Aramco Aviation, Nov. 6, 2007.

[5] Hamed, A., Tabakoff, W., and Wenglarz, R., **"**Erosion and Deposition in Turbomachinery," *AIAA Journal of Propulsion and Power*, Vol. 22, No. 2, March–April 2006.

[6] Tabakoff, W., and Simpson, G., "Experimental Study of Deterioration and Retention on Coated and Uncoated Compressor and Turbine Blades," AIAA Paper 2002-2373, Jan. 2002

[7] Abedi, M., "Effect of Restitution Coefficient on Inertial Particle Separator's efficiency," *Mechanical Engineering Master's Theses, Northeastern University,* Paper 17, 2009. http://hdl.handle.net/2047/d1001925x

[8] Vittal, B. V. R., Tipton, D. L., and Bennett, W. A., "Development of an Advanced Vaneless Inlet Particle Separator for Helicopter Engines," *AIAA Journal of Propulsion and Power*, Vol. 2, No. 5, 1986, pp. 438-444.

[9] Breitman, D. S., Dueck, E. G., and Habashi, W. G., "Analysis of a Split-Flow Inertial Particle Separator by Finite Elements," *AIAA Journal of Aircraft*, Vol. 22, No. 2, 1985, pp. 135-140.

[10] Zedan, M., Mostafa, A., Hartman, P., and Sehra, A., "Viscous Flow Analysis of Advanced Particle Separators," *AIAA Journal of Propulsion and Power*, Vol. 8, No. 4, 1992, pp. 843-848.

[11] Dai, L., Yu, M., and Dai, Y., "Nozzle Passage Aerodynamic Design to Reduce Solid Particle Erosion of a Supercritical Steam Turbine Control Stage," *Wear*, Vol. 262, 2007, p. 104–111.

[12] Eppler, R., *Airfoil Design and Data*, Springer – Verlag, New York, 1990.

[13] Selig, M. S., and Maughmer, M., "Multipoint Inverse Airfoil Design Method Based on Conformal Mapping," *AIAA Journal*, Vol. 30, No. 5, May 1992, pp. 1162-1170.

[14] Saeed, F., and Selig, M. S., "A Multipoint Inverse Airfoil Design Method for Slot-Suction Airfoils," *AIAA Journal of Aircraft*, Vol. 33, No. 5, Jul.–Aug. 1996, pp. 708-715.

[15] Selig, Michael S., "PROFOIL – A Multipoint Inverse Airfoil Design Method, User's Guide", Cleveland Ohio, Feb. 1999.

[16] Saeed, F., Al-Garni, A. Z., "Analysis Method for Inertial Particle Separator," *AIAA Journal of Aircraft*, Vol. 44, No. 4, Jul.–Aug. 2007, pp. 1150-1158.

[17] Al-Faris, E., and Saeed, F., "Design and Optimization Method for Inertial Particle Separator Systems," *AIAA Journal of Aircraft*, Vol. 46, No. 6, Nov.-Dec. 2009, pp. 1919-1929.

[18] Abolkhair, Y. M., "The Size Characteristics of the Drifting Sand Grains in Al-Hasa Oasis, Saudi Arabia," *Geology Journal*, Vol. 11, No. 2, 1985, p. 131-135.

[19] Eastes, J. W., "Spectral and Physical Properties of Some Desert Soils: Implications for Remote Spectroscopic Terrain Analysis in Arid Regions," *Applied Spectroscopy*, Vol. 46, No. 4, 1992, p. 640-644.

[20] Gunn, R., and Kinzer, G. D., "The Terminal Velocity of the Fall of Water Droplets in Stagnant Air," *J. Meteor.*, 6, 243-248, 1949.

[21] Chen, X., McLaury, B. S., and Shirazi, S. A., "Application and Experimental Validation of a Computational Fluid Dynamics (CFD)-Based Erosion Prediction Model in Elbows and Plugged Tees," *Computers & Fluids*, Vol. 33, 2004, pp. 1251–1272.

[22] Fair, G., and Geyer, J., *Water Supply and Waste Water Disposal*, John Wiley, New York, 1954.

[23] Clift, R., Grace, J. R., and Weber, M. E., *Bubbles, Drops, and Particles*, Academic Press, New York, 1978.

[24] Flemmer, R. L. C., and Banks, C. L. "On the Drag Coefficient of a Sphere," *Powder Technology*, Vol. 48, No. 3, 1986, pp. 217–221.

[25] Haider, A., and Levenspiel, O., "Drag Coefficient and Terminal Velocity of Spherical and Nonspherical Particles.'' *Powder Technology*, Vol. 58, 1989, pp. 63–70.

[26] Turton, R., and Levenspiel, O., "A Short Note on the Drag Correlation for Spheres," *Powder Technology*, Vol. 47, 1986, pp. 83–86.

[27] Khan, A. R., and Richardson, J. F., "The Resistance to Motion of a Solid Sphere in a Fluid," *Chem. Eng. Commun*.,Vol. 62, 1987, pp. 135–150.

[28] Brown, P. P., and Lawler, D. F., "Sphere Drag and Settling Velocity Revisited," *Journal of Environmental Engineering*, Vol. 129, No. 3, March 2003, pp. 222-231.

[29] Chhabra, R. P., Agarwal, L., and Sinha, N. K., "Drag on Non-Spherical Particles: An Evaluation of Available Methods," *Powder Technology*, Vol. 101, No. 3, March 1999, pp. 288—295.

[30] Taslim, M. E., Khanicheh, A., and Spring, S., "A Numerical Study of Sand Separation Applicable to Inlet Particle Separator Systems," *Journal of the American Helicopter Society*, Vol. 54, No. 042001, 2009.

[31] Taslim, M. E., and Spring, S., "A Numerical Study of Sand Particle Distribution, Density, and Shape Effects on the Scavenge Efficiency of Engine Inlet Particle Separator Systems," *Journal of the American Helicopter Society*, Vol. 55, No. 022006, 2010.

[32] Laitone, J. A., "Characterization of Particle Rebound Phenomena in the Erosion of Turbomachinery," *AIAA Journal of Aircraft*, Vol. 20, No. 3, March 1983, pp. 275-281.

[33] Tabakoff, W., and Hamed, A., "Installed Engine Performance in Dust-Laden Atmosphere," AIAA Paper 84-2488, AISS/AHS/ASEE Aircraft Design Systems and Operations Meeting, San Diego, CA, Oct. 21–Nov. 2, 1984.

[34] Tuncer, C., *An Engineering Approach to the Calculation of Aerodynamic Flows*, Horizon Publishing Inc. (Springer), California, 1999.

[35] Saeed, F., Brette, C., Fregeau, M., Trifu, O., and Paraschivoiu, I., "A Three-Dimensional Water Droplet Trajectory and Impingement Analysis Program," AIAA Paper 2005-4838, June 2005.

[36] Saeed, F., "State-of-the-Art Aircraft Icing and Anti-Icing Simulation," *ARA (American Romanian Academy) Journal*, Vol. 2000-2002, No. 25-27, June 2002, pp. 106-113.

[37] Langmuir, I., and Blodgett, K. B., "A Mathmatical Investigation of Water Droplet Trajectories," US Army Air Forces TR 5418, Feb. 1946 (Contract No. W-33-038-ac-9151 with General Electric Co.). Also US Department of Commerce Publication Board (PB) No. 27565.

[38] Bragg, M. B., "A Similarity Analysis of the Droplet Trajectory Equation," *AIAA Journal*, Vol. 20, No. 12, Dec. 1982, pp. 1681-1686.

[39] S. L. Wells, M. B. Bragg, "A Computational Method for Calculating Droplet Trajectories Including the Effects of Wind Tunnel Walls," AIAA 92-0642, January 1992.

[40] Tran, P., Brahimi, M. T., and Paraschivoiu, I., "Ice Accretion on Aircraft Wings," *Canadian Aeronautics and Space Journal,* Vol. 40, No. 3, Sept. 1994, pp. 91-98.

[41] Fehlberg, E., “Classical Eighth- and Lower-Order Runge-Kutta-Nyström Formulas with a New Stepsize Control Procedure for Special Second-Order Differential Equations,” NASA Technical Report R-381, March 1972.

[42] Reklaitis, G. V., Ravindran, A., and Ragsdell, K. M., *Engineering Optimization: Methods and Applications*, Wiley-Interscience, 1983.

[43] MATLAB 7.0, The MathWorks, Inc., Natick, MA, 2008 http://www.mathworks.com/ (retrieved 10 April 2010).